Atmospheric Correction of ASTER

K. Thome, F. Palluconi, T. Takashima, and K. Masuda

Abstract—An atmospheric correction algorithm for operational use for the high-spatial resolution, Advanced Spaceborne Thermal Emission and Reflection Radiometer (ASTER) is presented. The correction is a straightforward approach relying on inputs from other satellite sensors to determine the atmospheric characteristics of the scene to be corrected. Methods for the solar reflective and thermal infrared (TIR) are presented separately. The solar-reflective approach uses a lookup table (LUT) based on output from a Gauss–Seidel iteration radiative transfer code. A method to handle adjacency effects is included that relies on model output, assuming a checkerboard surface. An example of a numerical simulation shows that the effect of a land surface on the radiance over the ocean is stronger just off the coastal zone and decreases exponentially with increasing distance from the land. A typical numerical simulation is performed over the Tsukuba lake area in Japan. The TIR approach relies on the radiative transfer code Moderate Resolution Atmospheric Radiance and Transmittance Model (MODTRAN). The code is run for a given set of atmospheric conditions for multiple locations in the scene for several representative elevations. Pixel-by-pixel radiances are then found using spatial interpolation. Sensitivity analysis of the methods indicate that the results of the atmospheric correction will be limited by the accuracies of the input parameters.

Index Terms— Advanced Spaceborne Thermal Emission and Reflection Radiometer (ASTER), atmospheric correction, lookup table.

I. INTRODUCTION

ONE of the objectives of the Advanced Spaceborne Thermal Emission and Reflection Radiometer (ASTER) is to provide estimates of the surface-leaving radiance by applying an atmospheric correction to the data. ASTER is a high-spatial resolution imaging spectroradiometer provided by the Japanese Ministry of International Trade and Industry to the National Aeronautics and Space Administration (NASA). It is part of NASA's Earth Observing System (EOS)-AM1 spacecraft [1], [2]. Details on the design and operation of ASTER can be found in other sources [3]–[5], but key elements to the atmospheric correction are given here. The

sensor has three subsystems: the visible and near-infrared (VNIR) with 15-m resolution, shortwave infrared (SWIR) with 30-m resolution, and thermal infrared (TIR) with 90-m resolution [6], [7]. Details on the bands and radiometric requirements are shown in Table I. The band 3N refers to the nadir-looking band and the identical band, 3B, views with a separate telescope in the aft direction for stereo imaging. The swath width of ASTER is 60 km, with cross-track pointing of 8.6° for the SWIR and TIR and 24.0° for the VNIR. ASTER continues the trend to higher spatial resolution surface imaging begun with the Landsat Thematic Mapper (TM) and Systeme Pour l'Observation de la Terre (SPOT) Haute Resolute Visible (HRV) cameras. Previous instruments with both solar-reflective and thermal bands, notably, the Advanced Very High Resolution Radiometer (AVHRR), TM, and the Heat Capacity Mapping Mission (HCMM), either have lower spatial resolution (AVHRR, HCMM) or provide single-channel thermal data (TM, HCMM). ASTER increases the number of bands relative to these sensors while providing high-spatial resolution and same-orbit stereo capability.

Atmospheric correction provides estimates of the radiation emitted and reflected at the surface, and it is necessary for observing parameters that are intrinsic to the surface. ASTER operates in two distinct spectral regions: the solar reflective (VNIR and SWIR bands), where the dominant source is reflected sunlight, and the TIR, where the dominant source is terrestrial emission. Thus, the atmospheric correction problem can be viewed as two distinct problems. For the solar reflective, accurate atmospheric correction removes the effects of changes in satellite-sun geometry and atmospheric conditions due to aerosol scattering [8]. Atmospherically corrected surface reflectance images improve the accuracy of surface-type classification [9], [10] and are a basis for estimating the radiation budget of the earth [11]. Full use of satellite data for agricultural resource management also requires atmospheric correction [12]. Past work in atmospherically correcting satellite data has been successful over the ocean because of assumptions about the spectral reflectance allow aerosol parameters to be determined [13], [14]. While the problem is more difficult over land, recently developed techniques hold the promise of accurate aerosol retrievals over land. A recent issue of the *Journal of Geophysical Research* contains a set of papers on atmospheric retrievals from satellite data and methods of atmospheric correction [15].

In the TIR, numerous, multichannel, empirical approaches have been developed to determine the surface-leaving radiance over water, and thus infer the sea-surface temperature [16]–[19]. These methods establish the relationship between water temperatures measured at the sea surface and the bright-

K. Thome is with the Remote Sensing Group, Optical Sciences Center, University of Arizona, Tucson, AZ 85721 USA (e-mail: kurt.thome@opt-sci.arizona.edu).

F. Palluconi is with the Jet Propulsion Laboratory, California Institute of Technology, Pasadena, CA 91109 USA.

T. Takashima is with the Earth Observation Research Center, NASDA, Minato-ku, Tokyo, 106 Japan.

K. Masuda is with the Meteorological Research Institute, Tsukuba-shi, Ibaraki, 305 Japan.

TABLE I
ASTER BANDS AND RADIOMETRIC SPECIFICATIONS

Subsystem (& detector type)	Band #	FWHM bandpasses	Radiometric resolution	Quanti-zation	1-σ calibration uncertainty
VNIR (Si-CCD 5000 × 4)	1	0.52-0.60	0.5%	8 bit	±4%
	2	0.62-0.69			
	3N, 3B	0.76-0.86			
SWIR (Cooled PtSi 2048 × 6)	4	1.60-1.70	0.5%	8 bit	±4%
	5	2.145-2.185	1.3%		
	6	2.185-2.225	1.3%		
	7	2.235-2.285	1.3%		
	8	2.295-2.365	1.0%		
	9	2.360-2.430	1.3%		
TIR (Cooled HgCdTe PC 10×5)	10	8.125-8.475	0.3 K	12 bit	3 K (200-024 K) 2 K (240-270 K) 1 K (270-340 K) 2 K (340-370 K)
	11	8.475-8.825			
	12	8.925-9.275			
	13	10.25-10.95			
	14	10.95-11.65			

ness temperatures measured in two or more strategically chosen spectral channels to include differential effects in atmospheric absorption and emission. While these methods provide good results over water, where the emissivity is relatively well known, they produce mixed results over land [20].

This paper describes the operational atmospheric correction that will be used for ASTER. The paper covers the correction of the VNIR/SWIR bands and the TIR bands separately. The VNIR/SWIR description includes a discussion of an adjacency-effect correction and the method that will be used in the absence of atmospheric information. Results of sensitivity analyses for both approaches follows the discussion of the methods that will be used.

II. ATMOSPHERIC AND TOPOGRAPHIC INPUTS

One issue for the atmospheric correction of ASTER is the fact that the system was not designed to retrieve atmospheric information. Because of this, the ASTER Science Team decided to rely on outside sources for atmospheric parameters for the at-launch version of the atmospheric correction. Most of these parameters will be obtained from results from other EOS-AM1 platform sensors, such as the Multi-angle Imaging SpectroRadiometer (MISR) and the Moderate-Resolution Imaging Spectroradiometer (MODIS). For the TIR, the most important factors are atmospheric water vapor and temperature, and MODIS products will be used when possible for profiles of temperature, humidity, and column water vapor. As a backup, we will interpolate results of global assimilation model data [21], [22].

Because of the placement of the ASTER channels, ozone is not a significant factor in atmospheric correction, except for channels 2, 11, and 12, which are in the Chappuis absorption band or are near the ozone band between 9 and 10 μm.

Profile information from the Stratospheric Aerosol and Gas Experiment (SAGE) is the first choice for columnar ozone, but SAGE II, or its replacement, may not be available at the start of the EOS-AM1 mission and MODIS results are a secondary source. We also plan to use ozone estimates from Total Ozone Mapping Spectrometer (TOMS) but these data, as well as the SAGE data, will not be coincident in space and time with the ASTER measurements. If no ozone estimates are available, or if the temporal differences between ozone measurements and ASTER data collection cause large uncertainties, we will rely on climatology based on the TOMS and SAGE data. Atmospheric scattering is often dominated by aerosols and are important for the solar-reflective bands of ASTER. Information on the aerosol type and amount will be derived from results from MISR. If these data are not available, we will rely on MODIS results or climatological data.

The atmospheric information needed for the calculation of the atmospheric correction will be at resolutions lower than that of ASTER. This is also true of the surface topographic data, where the only global digital elevation model (DEM) available for ASTER is ETOPO5, which has elevations posted approximately every 10 km [23]. The EOS project has plans to provide a near-global DEM with 1-km postings based on the Digital Chart of the World (DCW) and other sources [23]. The project is also examining 90-m posting data based on the Defense Mapping Agency's (DMA) Digital Terrain Elevation Data (DTED) [23].

III. SOLAR REFLECTIVE CORRECTION

A. Overview of Method

The atmospheric correction for the VNIR and SWIR is based on a lookup table (LUT) approach, assuming that

atmospheric scattering optical depths and aerosol parameters are known from outside sources. Using these parameters, a set of piecewise linear fits are determined from the LUT that relate the measured satellite radiances to surface radiance and surface reflectance. The method described here is similar to a scheme implemented for Landsat TM that relied on ground-based solar radiometers to characterize the atmosphere [24]. The reflectance of an arbitrary pixel in the TM image is corrected, assuming the relationship between the at-sensor radiance and surface reflectance is linear. This relationship is actually quadratic over the full 0.0–1.0 range of reflectance, but it is sufficiently linear over shorter ranges [25]. The satellite radiance derived from the image DN is matched to a pair of code radiances, and the corresponding reflectance factor is obtained by linear interpolation.

Application of this approach to TM imagery yielded uncertainties of 0.008 in reflectance over an agricultural area, with reflectance ranging 0.02–0.55 [24]. Application to HRV data, including off-nadir angles similar to those expected from ASTER, resulted in reflectances to better than 10% absolute error for the same agricultural area, with a 0.1–0.4 reflectance range [12]. A study of several atmospheric correction methods yielded better than a 0.015 rms error in reflectance over the range of 0.02–0.63 for a similar approach [26]. The same study also showed that this approach compares favorably with other methods. The above technique has only been used on subscenes on the order of 512 × 512 pixels and never operationally because it is too computationally intensive. Using an LUT approach reduces computational requirements, and LUT's avoid the complexity of maintaining radiative transfer codes in an operational environment [8]. LUT approaches have been used successfully over water [27], [28], and land [29].

The actual atmospheric correction begins by using inputs of columnar amounts of absorbing gases to compute the transmittance for the ASTER bands using a modified form of the program Moderate Resolution Atmospheric Radiance and Transmittance Model (MODTRAN). The satellite radiances are divided by these transmittances. While this is a crude approach, it should be sufficient for typical surface targets and the low absorption in the ASTER bands. The scattering optical depths and aerosol type obtained from climatology or results from MISR or MODIS measurements are used to determine the appropriate portion of the LUT. In most cases, the values of the input parameters to the atmospheric correction will not match those of the LUT. For cases in which enough radiative transfer code runs can be stored in the LUT so that there is less than a 1% difference between cases, we simply use the nearest LUT case. The molecular scattering optical depth and view angle are treated in this fashion. When it is too computationally expensive to generate the large number of runs needed to keep differences to less than 1%, then linear interpolation of the LUT cases is used. The solar zenith and aerosol scattering optical depth are treated in this manner. Once the appropriate surface radiances, reflectances, and sensor radiances are determined from the table, piecewise linear fits are calculated. The ASTER radiance is then used with the proper linear fit to determine the surface radiance and reflectance.

B. Radiative Transfer Code

The radiative transfer code used to calculate the radiances for the LUT is a Gauss–Seidel iteration code that assumes the earth is flat with a homogeneous, Lambertian surface and a plane-parallel, homogeneous atmosphere divided into optically thin layers [30]. The input parameters for the radiative transfer code include solar zenith angle, surface reflectance, and desired view angle. Other inputs include molecular and aerosol scattering optical depths, aerosol index of refraction, and aerosol size distribution. The code is efficient computationally, but even so, it is not feasible to run the code on an operational basis for atmospheric correction of ASTER data. For a typical 60 × 60-km ASTER scene, it is reasonable to divide the scene into 5 × 5 areas, where atmospheric composition is assumed constant. Then 25 runs of the radiative transfer code are needed for each of the nine VNIR/SWIR bands. If five reflectance values are calculated per band to obtain the piecewise linear fits, the total number of runs needed is 1125. On a typical workstation, this translates to several hours to perform the radiative transfer calculations. Thus, we need computers that are several orders of magnitude faster, fewer runs of the radiative transfer code, or an LUT. It was decided to use an LUT because it gives us an efficient means to solve the problem without sacrificing too much accuracy.

C. LUT Resolution

The goal of selecting parameters to generate the LUT is to develop the smallest table possible while still producing accurate results. While the access time for the LUT does not strongly depend upon the size of the table because the results are stored in a relational database [31], a smaller table requires less time to generate. A study of the sensitivity of the top-of-the-atmosphere (TOA) radiances to LUT parameters was done to determine the values needed to generate a table in which changes in the input parameters cause a percent change in the at-sensor radiance of less than 1%.

When this philosophy was applied to the wavelengths of ASTER, it was found that only two wavelengths are required to generate the LUT, one for the VNIR (band 2) and one for the SWIR (band 5). Changes in wavelength have two effects on the radiative transfer for a given set of optical thicknesses. One is the scattering phase function. The wavelength effect is small when compared to uncertainties in the phase function caused by uncertainty in the size distribution and index of refraction. An additional effect is that the single scattering albedo is wavelength dependent. If the single scattering albedo is known for each band, this wavelength effect can be partially corrected. Figs. 1 and 2 illustrate these effects. Fig. 1 shows the percent change in the scattering phase function between the upper and lower wavelengths of both the VNIR and SWIR telescopes for a Junge parameter of 3.0, real index of refraction of 1.44, and imaginary index of 0.03. This figure represents one of the more severe cases, yet still shows phase function differences of less than 1% for scattering angles between the solar beam and the view angles of ASTER. The larger effects at other scattering angles are mitigated by multiple scattering. Fig. 2 shows the percent change in radiance between the wavelengths
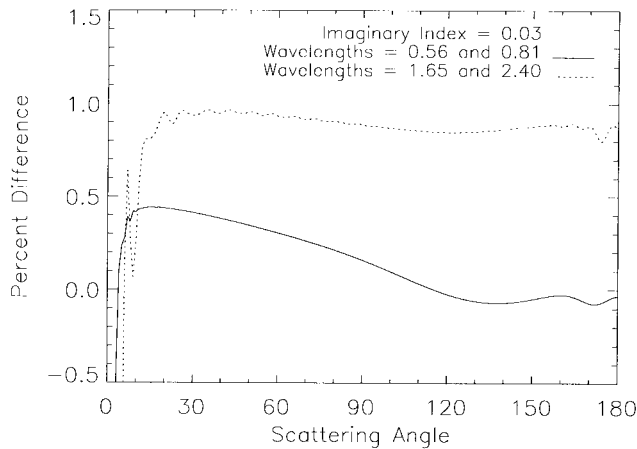
Fig. 1. Percent difference in Mie scattering phase function $(100 \times [P(\lambda_1) - P(\lambda_2)]/P(\lambda_1))$ determined for the upper and lower wavelengths of both the VNIR and SWIR telescopes.
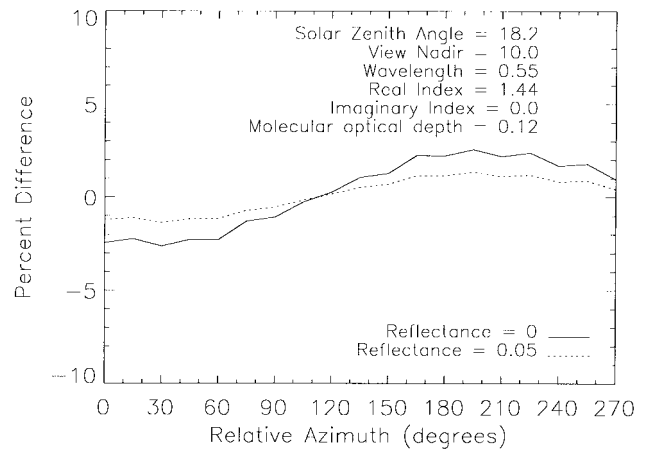

Fig. 3. Percent difference of at-sensor radiances $(100 \times [L(\phi_1) - L(\phi_2)]/L(\phi_1))$ for 15° intervals in relative azimuth for low reflectances.
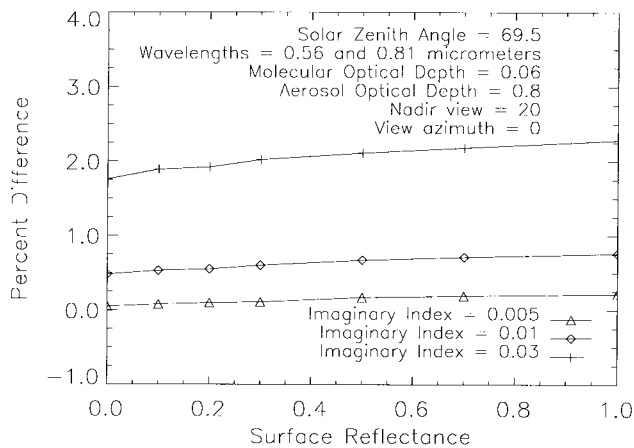

Fig. 2. Percent difference of at-sensor radiances $(100 \times [L(\lambda_1) - L(\lambda_2)]/L(\lambda_1))$ between the upper and lower VNIR wavelengths with other parameters held constant.

Fig. 4. Percent difference of at-sensor radiances $(100 \times [L(\phi_1) - L(\phi_2)]/L(\phi_1))$ for 15° intervals in relative azimuth for low- and high-aerosol optical thicknesses.

of bands 1 and 3 as a function of surface reflectance when the scattering optical depths are held constant. Similar results are obtained for bands 4 and 9. In this figure, the aerosol optical depth is assumed to be 0.8. The effects are similar for other optical depths. About 0.5% of the effect seen can be attributed to differences in the single scattering albedo. By selecting the middle wavelength for each spectral region and adjusting for imaginary index effects, the percent error from using one wavelength is in the 0.5–1.0% range.

The effect due to azimuth angle depends strongly on surface reflectance. For reflectances greater than 0.3, we found that a 15° interval is acceptable. At reflectances less than 0.3, a smaller difference is required when the view zenith is greater than 10°. For view zenith angles <10°, a difference of less than 15° is not required, except for reflectances less than 0.2. Figs. 3 and 4 illustrate some of these effects. Fig. 3 shows the percent difference in at-sensor radiance due to a 15° change in azimuth angle for the conditions listed in the graph. The feature to notice is that the uncertainty for a surface reflectance of 0.05 is nearly one-half the value for a reflectance of 0.0. The uncertainty becomes much smaller as the reflectance continues
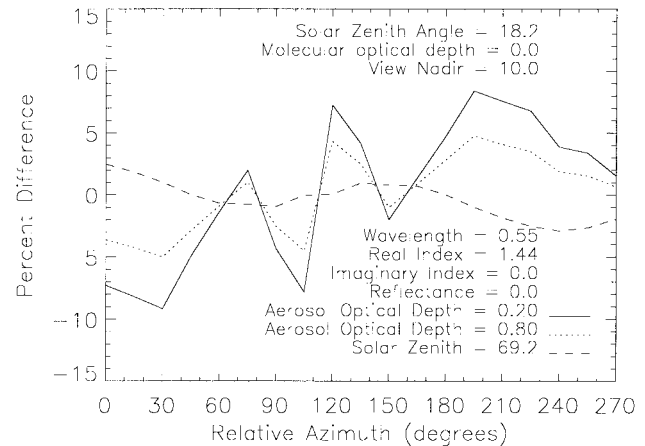
to increase. Fig. 4 is similar to Fig. 3, except two optical depths are presented. Because of the nature of the radiance as a function of azimuth, using an interpolation scheme does not reduce the uncertainty. Thus, values selected for generating the LUT are 0–180° at 15° intervals for reflectances larger than 0.1, and an interval of 7.5° has been selected for reflectances of 0.0 and 0.1.

While the relative azimuth (or equivalently, the view azimuth) is not a well-behaved function, the view nadir angle is better behaved. In general, the interval should not exceed 2° to satisfy the accuracy requirements for a nearest-case approach. It is possible to have larger intervals for cases of high surface reflectance, small solar zenith angle, and low turbidity. Based on this and the known pointing limitations of the sensor, view angles have been selected that have a 1° interval from 0 to 9° for the SWIR band and 0–24° at 1° intervals for the VNIR band.

The change in at-sensor radiance with changing solar zenith angle is straightforward. The requirement is that the interval in solar zenith must be less than 0.01 in the cosine of the solar zenith to ensure that the percent change in at-sensor radiance is less than 1% for a nearest-case method. Because

it is unrealistic to use a cosine interval of 0.01, thus requiring 66 values for solar zenith angle for the range from 0 to 70°, the current approach uses interpolation techniques to account for changes in solar zenith. We are using 15 values for solar zenith angles ranging from 0 to 72.5° at 0.05 intervals in cosine. Work is still being done to determine the optimal method for handling solar zenith angles larger than 72.5°. This is complicated by the fact that at larger solar zenith angles the assumption of the earth-atmosphere system being plane-parallel begins to break down.

The aerosol optical depth results are highly dependent on the surface reflectance. For reflectance greater than 0.0, differences are less than 1% for differences in aerosol optical depth of 0.025. Interpolation on results for a 0.15 interval results in differences of less than 0.3%. The maximum value for the aerosol optical depth that will be used is 0.9. Values larger than this cause the Gauss–Seidel iteration method to breakdown and not converge to a solution. It was decided to accept this constraint because familiarity with the Gauss–Seidel code allows for easier development. In addition, the use of an operational code for cases of such high turbidity is not recommended and these cases will receive special processing. Results of studies of the molecular optical depth are essentially identical to those for aerosol optical depth, but a 0.15 interval covers the entire range of expected molecular optical depths for ASTER. A nearest-case approach is adopted for molecular scatter with 13 values of molecular optical depth, 0.01 to 0.13 at 0.01 intervals for the VNIR and one value of 0.002 for the SWIR bands.

The final parameter is surface reflectance. Since the approach uses linear interpolation to retrieve reflectance from at-sensor radiance, we examined only the differences due to interpolation. Values of 0.0, 0.1, 0.2, 0.3, 0.5, 0.7, and 1.0 are adequate with interpolation causing less than 0.2% differences.

D. Adjacency Effect

The radiance at the sensor while viewing a specific site is affected by atmospheric scattering from adjacent areas to the site, and several useful papers have been published since the late 1970's on this topic [32]–[35]. Tanre *et al.* [36] expresses the at-sensor radiance as a sum of the radiative interactions between the atmosphere and a Lambertian surface. A total of six interaction terms using an average environmental reflectance accounts for more than 85% of the total adjacency effect. Takashima and Masuda [37] consider nine terms with a Lambertian surface and show that the adjacency effect depends on scene contrast, spatial resolution of the sensor, and the optical properties of the atmosphere. Because it is largest for high-spatial resolution sensors, large atmospheric scattering optical thicknesses, and high-contrast scenes, it must be taken into account to properly determine the surface reflectance and radiance for ASTER. Because of the complicated nature of determining the contribution of radiation from adjacent regions, the problem is difficult to treat on an operational basis. However, the multispectral data at the high-spatial resolution of ASTER should allow for an adjacency correction in the atmospheric correction of ASTER data.

For the model presented here, we assume a plane-parallel, stratified atmosphere, where the scatterers are constant within a layer. If the surface reflectance is spatially varying, the reflection function for the earth-atmosphere system can be expressed in a form consistent for use in a doubling-adding radiative transfer code as

$$S_R(\delta) = S(\delta) + \frac{[\exp(-\delta/\mu) + T(\delta)]R_s(A, v_{\text{wind}})}{1 - S(\delta)R_s(A, v_{\text{wind}})}$$
$$\cdot [\exp(-\delta/\mu_0) + T(\delta)]$$

where $S_R(\delta)$ is the normalized radiance at the sensor for an optical thickness of δ [38], S and T are the reflection and transmission functions of the atmosphere, μ and μ_0 are the cosine of the view and solar zenith angles, A is the surface albedo, v_{wind} is the surface wind speed, and R_s is the surface reflection function. The denominator indicates an infinite series of hemispherical radiative interactions between the surface and the atmosphere. Including the first nine of these interactions for optical thicknesses, less than 2.0 ensures uncertainties less than 1% [38].

We simulate the heterogeneous surface as a checkerboard with uniform surface properties within a given square [39]. Because the multiply-scattered energy from areas adjacent to the target is difficult to derive, we divide this process into three parts. First, is the forward-scattered energy from the surface within the sensor's instantaneous field-of-view (IFOV). Second, radiation is scattered from within the sensor's IFOV outside the IFOV and back into the IFOV by atmospheric constituents. Third, radiation reflected by adjacent pixels is scattered into the IFOV. The contribution of the first part is large because of the strong forward scattering by aerosol; the second and third parts are relatively small. Also, as the distance from the target pixel increases, the optical thickness of the slant path from the adjacent pixel to the sensor IFOV becomes larger and the contribution of the adjacent pixel to the target pixel decreases due to attenuation.

The model assumes the ratio of the diffusely transmitted radiation from the adjacent pixel to the target pixel is identical to that computed for single scattering. This emphasizes the relative position of each respective pixel to the target rather than the precise radiative transfer processes in the atmosphere. This ratio, of course, decreases with increasing distance from the target since the attenuation of the transmitted diffuse radiation increases with the distance. Accuracy is improved if the interaction of radiation in and out of the IFOV is considered for the second and higher order scattering, but this increases the computational complexity. To evaluate the adjacency effect, we will refer to two parameters α_i and β_i, which are ratios related to the singly-scattered radiation from an adjacent ith pixel in the heterogeneous case to that from a one-dimensional (1-D) system. The ratio of the diffusely transmitted radiation is α_i and the diffusely reflected situation is β_i. The sums of α_i and β_i over all adjacent pixels (over all values of i) should have a value of 1.0 for the best accuracy.

We determine radiances using both a 1-D model with homogeneous surface and the checkerboard model. The optical thickness for molecular scattering and absorption for the simu-
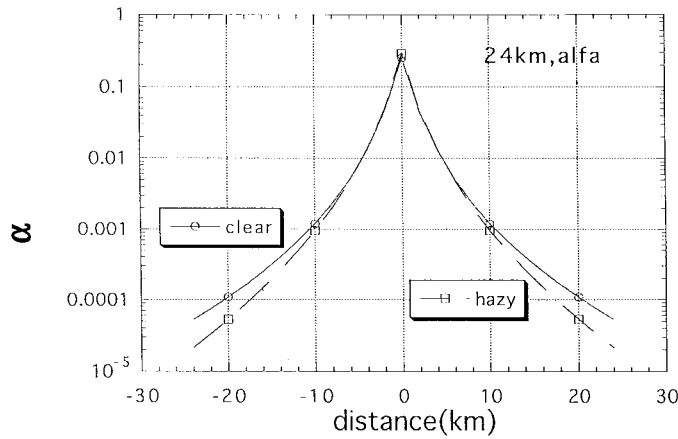
Fig. 5. Parameter α as a function of distance from the target pixel indication adjacency effects on the observed radiance for a target at nadir for clear and hazy conditions.
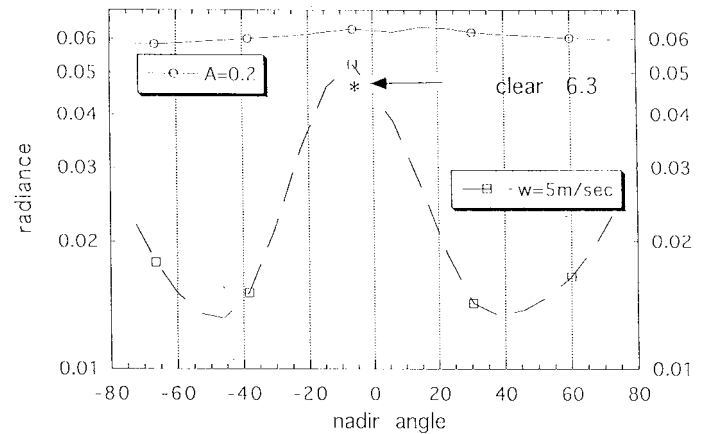

Fig. 6. Comparison of the radiance calculated by the doubling-adding method for a homogeneous surface to that by the present method including adjacency effects. The atmosphere is assumed to be clear, and the solar zenith is 6.3°.

lations are from LOWTRAN7 [40] for the summer midlatitude model. The aerosols are assumed to be dust-like particles [41] represented by a log-normal distribution of spherical particles with a mean radius of 0.5 μm and a standard deviation of 2.99 μm. The refractive index at a wavelength of 0.55 μm is 1.53–i0.008. The Selby and McClatchey vertical distribution [42] is modified so that the total aerosol optical thickness (δ) is 0.1 at 0.55 μm for a clear atmosphere and 0.35 for the hazy case. The single scattering phase function is calculated from Mie theory for radii between 0.001 and 10 μm, and total optical thicknesses are tabulated for ASTER's VNIR bands.

In the present simulation, the sum of the αs is found to be 0.93 and for the βs to be 0.76 for the clear atmosphere case for band 1. The values are 0.94 and 0.75 in hazy conditions. While α is nearly one, β is much lower, but this is not problematic because of the relatively small contribution, as compared to the diffusely transmitted component, of diffusely reflected radiation from adjacent pixels to the target pixel radiation. It is possible to improve these sums by adopting a larger area over which to consider adjacency effects and smaller checkerboard pixel size, but this increases the computational complexity of the problem. As an exercise, we examine how large an area might be needed to improve the sums by determining the contribution of scattered radiation from adjacent pixels as a function of distance from the observation direction. Fig. 5 shows the value of α as a function of distance and that the contribution from adjacent pixels is less than 1% at a distance of 10 km and less than 0.1% at 20 km for the clear case. In the hazy case, these percentages are lower. That is, the contribution decreases faster with distance in hazy conditions. Again, this is because of greater attenuation of the adjacent pixel's radiation in hazy conditions.

As a check of the model's numerical accuracy, we determined radiances at the TOA for the case of a homogeneous water surface using both a doubling-adding code and the current approach. Fig. 6 shows the upwelling radiance as a function of angle from the water surface as well as that from a Lambertian surface for reference. The solid line indicates the upwelling radiation from a Lambertian ground surface with reflectance of 0.2, and the dashed line indicates the upwelling

radiation from an ocean with a surface wind of 5 m/s using the Cox–Munk model wave-slope model. For these results, the clear atmosphere case is used for Band 1 of ASTER. The solar zenith is 6.3°, explaining the peak in the curve at this view angle due to specular reflection. The radiance from the adjacency effect code is indicated on the graph by the * symbol and is 8.5% smaller than that from the doubling–adding code. In this case, the checkerboard size was 21.4 × 21.4 km with a homogeneous ocean surface. If the size of the checkerboard is taken to be 44.8 × 44.8 km, the difference becomes −6.5%. A similar result is obtained for a solar zenith angle of 60°.

Simulations have also been done for a test site that is planned for the validation of the atmospheric correction. The site is Kasumi-ga-Ura Lake in the Tsukuba area of Japan, about 60 km northeast of Tokyo. For the simulation, we consider adjacency effects up to a distance of 20 km from an assumed subsatellite point. The solar azimuth is 20.8 from the anticipated orbital inclination of ASTER for a local overpass time of 10:30 a.m. Two solar zenith angles are used, corresponding to those at the summer (13°) and winter (60°) solstices. The land surface is Lambertian, and the lake surface follows the Cox–Munk model wave-slope model for surface wind of 5 m/s. The vertical profile of aerosols and molecules is assumed to have an equivalent height of 7 km for the mixture of these constituents. The grid size is 1 × 1 km. Fig. 7(a) shows an enlargement of the middle of the lake (the subsatellite point is indicated by a "+" in the figure) with contours of percent change in at-sensor radiance over the water with a land boundary from that determined by assuming the target is homogeneous. Both the clear and hazy cases are shown. Fig. 7(b) shows a similar set of contours, but for the effect of the adjacent lake on the upwelling radiation from the land area. As expected, the effect of the lake on the upwelling radiation decreases with increasing distance from the lake. At a distance of 1 km from the lake, the difference is −1% from that of the homogeneous land surface in the clear condition and −2% for the hazy conditions. Also, the effect of the lake on the radiance over the land surface is smaller than the effect of the land on the radiance over the lake.
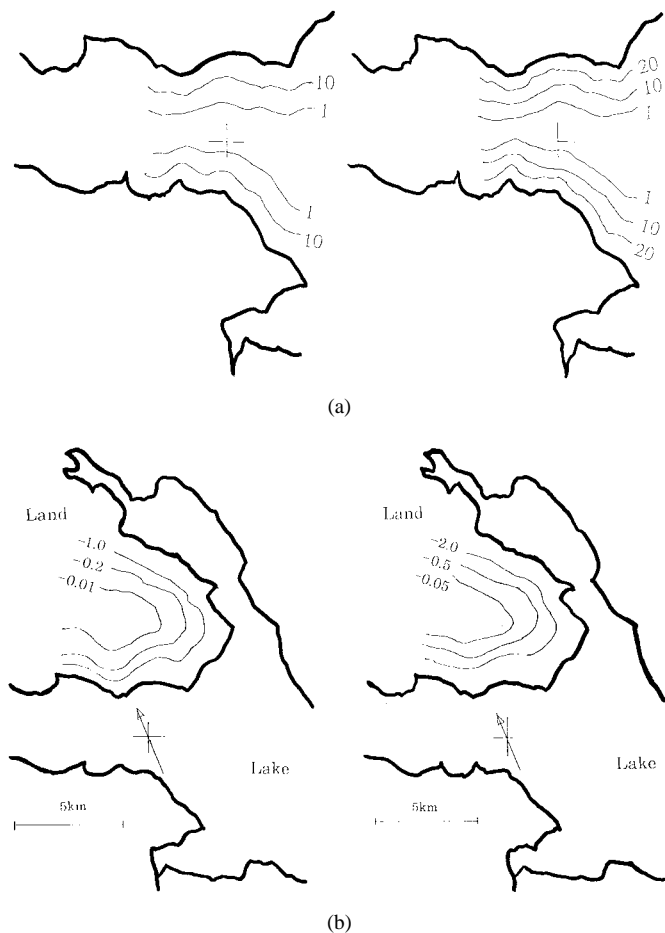
Fig. 7. (a) Contours of percent difference between radiances computed over a water target with and without including adjacency effects due to upwelling radiation from the nearby land surface. Results are for ASTER Band 1 for (left) clear and (right) hazy conditions. (b) Contours of percent difference between radiances computed over a Lambertian land target with and without including adjacency effects due to upwelling radiation from the nearby water surface. Results are for ASTER Band 1 for (left) clear and (right) hazy conditions.

Fig. 8. Flow diagram showing the planned atmospheric correction including adjacency effects.

These results indicate the importance of the adjacency effect for an ASTER correction. Fig. 8 shows a flow diagram for the proposed operational procedure of atmospheric correction. Because this correction is for use in an operational environment, application of the adjacency correction is limited to those cases in which the surface heterogeneity causes the adjacency effect to cause a change in retrieved surface reflectance of 3% at reflectances greater than 0.2 and 0.006 reflectance units for low reflectance. As will be seen in the section on uncertainties, this applies the adjacency correction to cases in which the uncertainty caused by ignoring the adjacency effect would exceed the uncertainties, due to the use of an LUT.

Ideally, we would like to include all contributions from all pixels to determine the correction for adjacency effects for ASTER. However, this is simply not feasible in an operational method. If the contribution of the width of 20 km is considered, the total number of adjacent pixels becomes 2666 × 2666 for the case of the VNIR subsystem of ASTER. Therefore, substantial computation time would be required if all of these pixels were considered. Thus, a checkerboard size will be selected based on the distance between the target and adjacent
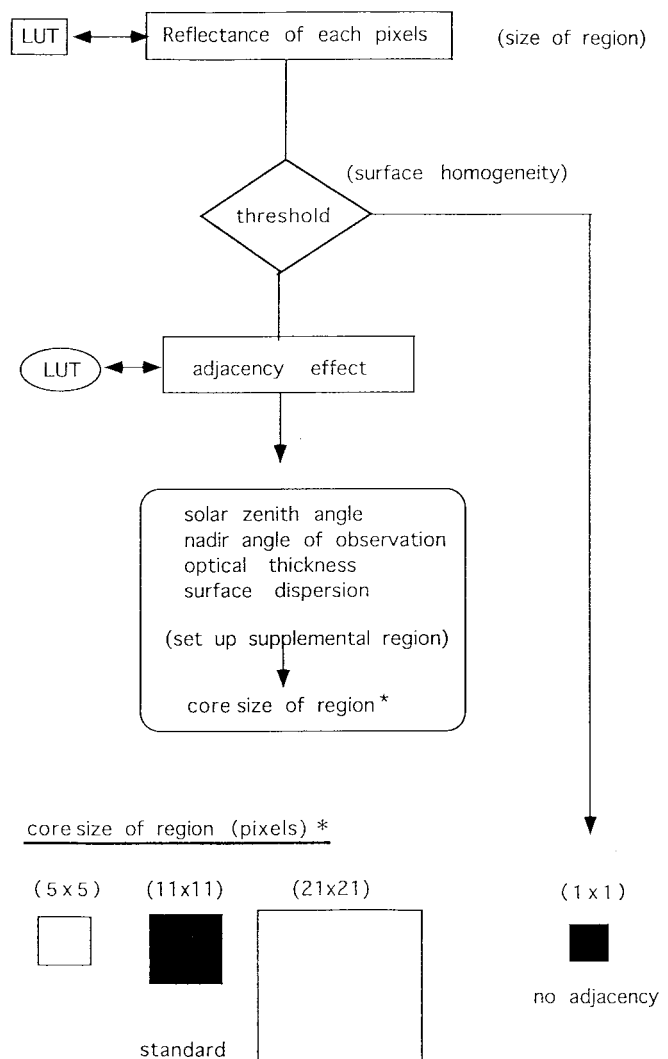
pixels to reduce this computation time. Preliminary work indicates that adequate results are obtained with as few as 441 pixels. One other problem is that accurate profile data of the scatterers cannot be provided for ASTER data. Therefore, we will adopt an equivalent height, where the optical properties equal those of an homogeneous atmosphere is introduced for the runs that are used to generate the adjacency correction LUT.

E. Atmospheric Correction in the Absence of Atmospheric Data

The atmospheric correction presented relies on aerosol information from sources outside the ASTER data stream. If no concurrent aerosol information is available, we rely on climatological values determined as a function of location. In parallel with the development of the LUT atmospheric correction approach, we continue to investigate other methods for cases with no outside data. The problem with such an approach is that the ASTER bands were not selected for the purpose of determining atmospheric characteristics. ASTER

does, however, have the advantage of having high spatial resolution and several bands in the SWIR, and this makes it suitable for an approach using ground targets of known reflectance. We are implementing an approach similar to that of the MODIS atmospheric group [43]. In this method, SWIR data are used to determine areas of low reflectance due to dark vegetation or water. These areas correspond to areas of low reflectance in the VNIR that can then be used to determine the aerosol properties [44]. For MODIS, it has been proposed that bands at 3.9 and 2.1 μm will be used to determine the reflectance at 0.47 and 0.66 μm. ASTER does not have a band at 3.9 μm, but has several possible bands in the SWIR that can be used. The primary disadvantage to using ASTER data to determine aerosol properties is the lack of a band in the blue portion of the spectrum. A secondary LUT is being developed, such that dark-pixel data in the VNIR bands are used to directly determine the surface reflectance and radiance without determining the aerosol characteristics explicitly.

IV. TIR CORRECTION

A. Description of Method

In the TIR, the radiance leaving the surface L_{sur} is a combination of both emission and reflection and is related to the at-sensor radiance L_{sen}, transmission of the atmosphere τ_r, and the atmospheric path radiance L_{path} (which arises from both atmospheric emission and scattering) as

$$L_{\mathrm{sat}} = L_{\mathrm{sur}} \times \tau_r + L_{\mathrm{path}}.$$

If the spectral emissivity of the surface is known, these two components can be separated. As mentioned, numerous, multichannel, empirical approaches have been developed to determine the surface-leaving radiance over water, in which the spectral emissivity can be assumed to be known. The major advantage of multichannel methods is they use measurements from the time and place of interest and inherently account for the atmosphere on a pixel-by-pixel basis.

For ASTER, such multichannel approaches will not be used because 1) the ASTER TIR channels were selected to avoid atmospheric effects, 2) the spectral emissivity of the land surface is not known and is highly variable, and 3) the multichannel method is sensitive to measurement noise. The effect of spatial emissivity variations on two-channel (split-window) methods has shown that the methods require both an absolute knowledge of the mean emissivity of the channels used as well as the difference in emissivity in the two bands [45]. For AVHRR channels 4 and 5, the mean emissivity must be known to 0.005 and the difference in emissivity to 7×10^{-4} for the error in the surface temperature derived to be of order 0.5 K. In general, the emissivity of the land surface is not well known. A study of effects of uncertainties in the at-sensor radiance on multichannel methods for AVHRR channels 3–5 show errors in channel brightness temperature are multiplied by six for a two-channel case and three for a three-channel case [46]. The approach by the MODIS Team is a multichannel method, but the MODIS bands, integration

times, and specified SNR were selected in part with such a method in mind [46].

Rather than a multichannel method, we use a "clear sky" correction. Among the issues in this scheme are 1) selecting an adequate atmospheric radiative transfer model for calculating path transmission and radiance, 2) finding sources of atmospheric information needed for the transfer model, and 3) preparing parameter sets compatible with the transfer model by merging and interpolation from the various sources. The basic approach is straightforward. The atmospheric parameters are derived from outside sources. These results are interpolated to a uniform grid (for example, 15-km grid point spacing) across an ASTER scene (60 × 60 km), including elevation effects. The atmospheric correction is calculated for each grid point (a total of 125 points for the five ASTER bands) for several elevations representative of the surrounding terrain. The correction appropriate for each pixel is obtained by a spatial interpolation from the surrounding grid points. The selection of the grid spacing is based on keeping the interpolation error to an acceptable level without requiring an excessive number of computations.

B. Radiative Transfer Code

The radiative transfer code for this approach should

1) have sufficient accuracy to meet the goals of the experiment;
2) be widely and easily available;
3) have community interest in making improvements to the code;
4) have previous use for atmospheric corrections in the TIR; and
5) be computationally efficient.

Based on these criteria, we selected MODTRAN because it has the properties above and because we have used it, in its several versions, for more than ten years. MODTRAN3 [47], [48] is the version currently included in the correction. MODTRAN, a successor to LOWTRAN, includes all the functional capabilities of LOWTRAN7 but uses a more accurate and higher resolution molecular band model, with 2-cm^{-1} resolution based on the HITRAN molecular database [49]. Thus, MODTRAN provides sufficient spectral resolution to be used with the narrowest ASTER TIR channels. Occasionally, updates to the code are provided by the developers, and we intend to evaluate each of these updates to determine whether it is warranted to update the atmospheric correction code with the new version. For example, at the time of the writing of this paper, MODTRAN4 was close to being released, and it will be evaluated by the ASTER Team to determine whether the modifications impact the atmospheric correction of ASTER. If so, it will be included in the next release of the atmospheric correction code delivered to the EOS project.

The MODTRAN band model uses a stored spectral database for 12 (H_2O, CO_2, O_3, N_2O, CO, CH_4, O_2, NO, SO_2, NO_2, NH_3, and HNO_3) of the 13 (N_2 is handled more simply) molecules included, with band model parameters calculated for 1-cm^{-1} spectral bins at five temperatures between 200 and 300 K. The model includes effects due to multiple scattering

Source	Low Reflectance		High Reflectance	
	Error	Total Error	Error	Total Error
Sensor radiometric calibration	4%	4%	4%	4%
Scattering optical depth	0.05	8%	0.05	1%
Aerosol type		10%		5%
Surface height	100 m	4%	100 m	1%
LUT		3%		3%
Surface BRF		1%		1%
Inherent code accuracy		1%		1%
Total Error (root sum of squares)		14%		7%

Fig. 9. Uncertainty in at-sensor radiance due to an 0.05 change in aerosol scattering optical depth.

by molecules and aerosols and allows the user to specify profiles of temperature, water vapor density, ozone, aerosols (in three regions: boundary layer, troposphere, and stratosphere) and any of the other gases that may vary with time (e.g., CO_2). Transmittance comparisons between MODTRAN and the line-by-line code, FASCODE3P [50], for horizontal paths have shown agreement to better than 2%. Radiance comparisons made with an upward-looking interferometer using quality atmospheric parameter measurements have also shown agreement to better than 2% [48]. More work needs to be done involving comparisons between MODTRAN and transfer models of established accuracy in the mode in which the model is to be used for ASTER atmospheric correction (i.e., looking vertically through the entire atmosphere), but a comparison of this type between MODTRAN, LOWTRAN6, and LOWTRAN7 with ATRAD, an accurate multiple scattering radiative transfer model, showed differences in the 0.5–2% range for broad thermal bands [46]. These limited attempts at establishing the accuracy of MODTRAN indicate it should be suitable for use, but further work using the ASTER band passes is needed to establish the accuracy that can be expected.

V. UNCERTAINTY ESTIMATES

A. Solar Reflective

Table II lists the uncertainty sources we have identified for the atmospheric correction. The table shows results for a low-reflectance case (reflectance <0.1) and a high-reflectance case (>0.1). The reason for dividing the table is that many of the uncertainties depend strongly on reflectance. The error column is the error in the quantity listed in the source column. These values should be viewed as those that might be expected for this work, but postlaunch validation is required to determine
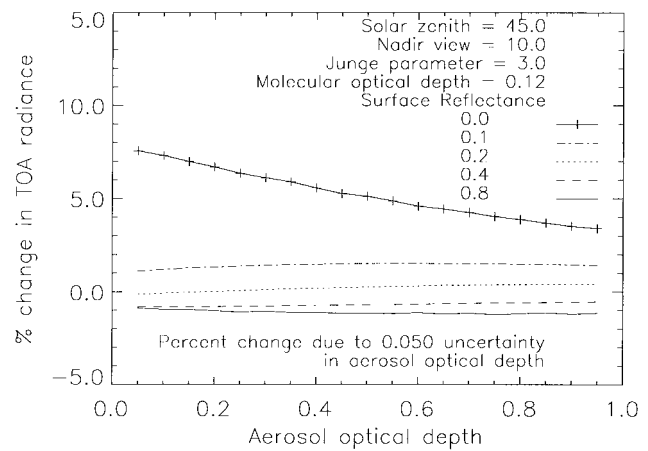
their actual values. The total error column is the error in at-sensor radiance in percent caused by the item in the source column. The overall total is the root sum of squares of all the error sources. The choice of the root sum of squares is not necessarily valid as the sources are known not to be independent in some cases. These tables are intended to indicate what parameters might cause problems when the atmospheric correction is implemented based on reasonable assumptions about the uncertainty of the inputs.

The first source of uncertainty listed in the tables is the sensor calibration related to the error in converting the satellite digital numbers to radiance. The specification for ASTER is 4%, absolute. In creating the summary tables, this value is assumed to be the same for both low and high values of reflectance, although this will not be the case. The LUT line in the table shows the largest expected uncertainty in computing the radiance using the LUT. If this value is exceeded, the LUT will be modified to reduce the uncertainty. Comparisons between independent radiative transfer codes making similar assumptions to that used to develop the LUT (Mie scattering by the aerosols, Junge size distributions, etc.) but different numerical techniques, give results that compare at the 1% level.

Another source of uncertainty is the scattering optical depth. Fig. 9 shows the percent difference in the at-sensor radiance due to an 0.05 change in optical depth. The results are shown as a function of optical depth for several surface reflectance values. The figure shows results for only one solar geometry and aerosol type, but similar results are obtained for other aerosol parameters and solar geometry. It can be seen that the sensitivity to optical depth is strongly dependent on the surface reflectance. When the surface reflectance exceeds 0.1, TOA radiance changes by less than 1% for optical depth uncertainties of 0.05. When the surface reflectance is less than 0.1, the uncertainty in TOA radiance can be as large as 8%.

Additionally, we must contend with uncertainties in the aerosol size distribution. For cases when other data from MISR and MODIS are available, these uncertainties should not be large because errors made in retrieving the aerosol types should cancel to some extent when applied to ASTER. The idea

is that, the aerosol type selected by the MISR and MODIS algorithms are those that best match the measured radiance distribution at the TOA. If these aerosol types are used in the ASTER case, they should at least accurately portray the atmospheric path radiances, allowing for a good reflectance retrieval. Still, it is expected that there will be an uncertainty due to this parameter, and the tables include reasonable values based on typical uncertainties in knowledge of a power-law distribution and uncertainty in imaginary index of refraction. Postlaunch validation will be used to better understand this.

Since the surface elevation is used to adjust the scattering optical depths, there are uncertainties due to the surface height derived from the input DEM. This is found to be 4% for the low-reflectance case and $<0.5\%$ for the high-reflectance case, for a height uncertainty of 100 m at sea level. Uncertainty due to surface slope is not included because it is not possible to assess this with the current radiative transfer code. In retrieving the surface radiance, we will not attempt to account for surface-slope effects because this would make the LUT prohibitively large. Rather, we use surface slope to adjust the retrieved surface reflectance. For a given slope error, the error in surface reflectance will be much larger as the slope angle increases. A $5°$ error in slope at $30°$ gives a 5% error in surface reflectance. The same $5°$ error at a slope angle of $45°$ is 8%. It should be noted that, since the radiative transfer code assumes a plane-parallel earth-atmosphere system, the uncertainties in the code results increase as the slope angle increases.

The LUT assumes the surface to be Lambertian for two reasons: 1) including bidirectional reflectance factor (BRF) effects in the LUT makes the table prohibitively large and 2) there is no BRF information available at the 30-m scale of ASTER. The effects of this assumption were investigated with the radiative transfer code for three surface BRF's. Case 1 used a surface having a factor for angles within $30°$ of the horizon that is ten times that of the nadir hemispherical-direct value. Case 2 simulated a hotspot effect with the reflectance factor in the backscatter direction being a factor of two greater than that for the nadir hemispherical-direct value. For these two cases, the solar angle was $45°$, thus, BRF effects only manifest themselves in the multiply scattered radiance at the sensor. Case 3 is identical to Case 2, except the sun angle is $18°$ and the hotspot is viewed directly.

Using these cases with a variety of hemispherical-directional reflectances, aerosol amounts and types, and view geometries, we determined the percent difference between the Lambertian and non-Lambertian cases. For all three of the above described cases, the percent difference from the Lambertian case was less than 1%, except the case when the sensor directly views the hotspot. In this case, the reflectance derived from the non-Lambertian radiances using a linear interpolation of the Lambertian results gives an error of 4–7% at low optical depths. This error is smaller at higher optical depths due to attenuation of the radiation from the hotspot. One BRF effect not examined is that due to specular reflection. While the current radiative transfer code can use a non-Lambertian surface, it does not treat specular reflection properly. The effect of specular reflection will be important for an ASTER-only atmospheric correction since small changes in the reflectance

of water will seriously affect the retrieved aerosol parameters.

The total uncertainty from all of these factors, assuming the component uncertainties in the table, is 14% for the low-reflectance case and 7% for the high-reflectance case. The error in the retrieved surface reflectance and surface radiance based on these results depends on the relationship between TOA radiance and surface reflectance and surface radiance. Using a moderate-turbidity case, the uncertainty in retrieved surface reflectance is 30–70% at a reflectance of 0.05. (or 0.02–0.04 units in reflectance). A 7% uncertainty leads to a 7–9% uncertainty in surface reflectance at a surface reflectance of 0.5 (or 0.04 units in surface reflectance). These values correspond well to those found using a similar atmospheric correction applied to TM [24] and HRV [12] at a low-turbidity agricultural site. These values are also similar in size to those found for several other atmospheric correction approaches [26]. Since these previous results used ground-based measurements of atmospheric parameters, they represent what we would expect in a best case. Thus, it is doubtful that using a more complicated atmospheric correction scheme will improve the uncertainties listed above, since it should be the uncertainty in the input parameters that is the largest source of uncertainty in the final result.

C. TIR

As with the VNIR/SWIR correction, the accuracy of the atmospheric correction method depends on the accuracy of the primary input variables and the sensitivity to their uncertainty. The primary input variables are atmospheric profiles for temperature, water vapor, ozone, and aerosols. Estimates for the sensitivity were developed prior to the release of MODTRAN using the LOWTRAN 7 radiative transfer code. The atmospheres used were midlatitude summer (air temperature at the surface 297.2 K, 2.35-cm column water amount, 0.332-cm-atm total ozone, and a "visibility" of 25 km), tropical [air temperature at the surface 302.7 K, 3.32-cm column water amount, 0.277-cm-atm total ozone and a "visibility" of 25 km], and Subarctic Winter (air temperature at the surface 257.2 K, 0.33-cm column water amount, 0.376 cm-atm total ozone, and a "visibility" of 25 km). The sensitivity to each variable, model atmosphere, and wavelength was determined by noting the change in radiance due to small changes in the base value of each of the four primary variables. The sensitivity in the ASTER Bands was obtained by weighting the wavelength-dependent sensitivities with the expected spectral profile of each ASTER channel. For this study, we assumed an uncertainty in columnar water vapor of 20%, 0.5% in atmospheric temperature, and 50% in column ozone and horizontal visibility. The results for three of the five ASTER channels in both radiance and brightness temperature are given in Table III for the two most sensitive atmospheres.

Because of strong water vapor absorption below 8 μm, ASTER Band 10 is about twice as sensitive to uncertainties in atmospheric water vapor and temperature as the other four bands. Band 12 is the most sensitive to uncertainties in ozone because of the presence of ozone absorption and gross errors

TABLE III
PERCENT CHANGE IN AT-SENSOR RADIANCE FOR THE TIR BANDS OF ASTER AS A FUNCTION OF PERCENT CHANGE IN THE GIVEN INPUT PARAMETER

Input Parameter	% Change in Input Parameter	% Change in Derived Radiance* for Tropical Atmosphere			% Change in Derived Radiance* for Mid-latitude Summer Atmosphere		
		Channel 10	Channel 12	Channel 13	Channel 10	Channel 12	Channel 13
Water Vapor	20	4.4 (2.2)	1.8 (1.0)	2.2 (1.5)	2.3 (1.5)	0.9 (0.5)	0.9 (0.6)
Atmospheric Temperature	0.5	-3.5 (-1.8)	-1.5 (-0.9)	-1.7 (-1.1)	-2.3 (-1.2)	-0.9 (-0.5)	-0.9 (-0.6)
Ozone	50	0.2 (0.1)	1.1 (0.6)	0.1 (0.1)	0.1 (0.1)	1.1 (0.6)	0.1 (0.1)
Visibility (Aerosols)	50	0.2 (0.1)	0.4 (0.2)	0.4 (0.3)	0.1 (0.1)	0.5 (0.3)	0.4 (0.3)

* Numbers in parenthesis ( ) are the changes in derived brightness temperature (K) which are equivalent to the percent change in derived radiance.

in ozone lead to errors greater than the instrument's $NE\Delta T$ for this band. Aerosols have a small impact on all five bands but little of this effect is due to the profile of the aerosols.

The simple sensitivity analysis presented here deals with errors that are biased consistently in one direction throughout the profile. As such, they should produce the largest error in radiance for a given assumed percentage error in one of the input variables. In practice, the error may vary with altitude, assume either sign within a given profile and the error from one source may partially balance that from another source. Also, the large number of parameters, in excess of 150, when considering profile information, necessary to set up an atmospheric model in MODTRAN, are correlated or anticorrelated to varying degrees in ways that are difficult to unravel. It may be that "standard" errors will be considerably less than the "maximum" errors that result from adding everything with the same sign. One general conclusion is that keeping the surface radiance error, due to errors in estimated water vapor and temperature profiles, below the 1-K accuracy of the ASTER instrument itself will be difficult for warm, humid atmospheres.

One source of uncertainty not covered in Table III is that due to elevation errors between the average elevation of the pixel of interest and the elevation used for that pixel in computing the atmospheric correction. The magnitude of the resulting error in the atmospheric correction depends on the atmospheric profile, elevation of the surface, surface temperature, and ASTER band being corrected. For five representative atmospheric profiles for all five ASTER TIR bands, the maximum error due to elevation uncertainty occurs in band 10 and is 0.3 K in brightness temperature for an altitude error of 100 m. Although the atmospheric correction error is not strictly linear with elevation error, the linear assumption is reasonably close for elevation errors up to several hundred meters. For Band 10, the most sensitive channel, the DCW elevation error of 650 m translates into the equivalent of a brightness error of 1.8 K for the worst case. The associated

error for a horizontal error of 600 m for a slope of 30° leads to a brightness temperature error of 0.8 K. For the DTED, the error due to vertical uncertainty is smaller than that from horizontal uncertainty and the error is 0.5 K from horizontal uncertainty with a 45° slope. For the majority of the earth's surface, the existing sources of topographic information should result in elevation-related atmospheric correction errors that are less than a few tenths of a degree Kelvin for the most sensitive ASTER band and atmospheric profile. In steep terrain (slopes greater than about 30°), it is likely the positional accuracy of both the elevation model and the ASTER pixels will determine the size of the error, and this could be more than 1.0 K in unfavorable cases.

Two additional points are also inherent in using an atmospheric profile-based atmospheric correction algorithm. First, this method is sensitive to artifacts in the topographic model used. Since global topographic data sets are necessarily large and have been compiled from a variety of sources, artifacts are inevitable. It is important to understand and remove these artifacts, where possible, as they will impose systematic position-based errors on the atmospherically corrected brightness temperatures. Second, topographic errors are not spectrally neutral across the five ASTER thermal channels. Methods that use the spectral contrast across these channels to extract additional information should, at a minimum, take into consideration the systematic effect topographic error will have on atmospherically corrected ASTER thermal data.

VI. CONCLUSION

A straightforward atmospheric correction is being developed for ASTER. The method relies on inputs on the state of the atmosphere from sensors better suited for such studies. The design of this atmospheric correction has focused on providing an accurate correction that is robust enough for an operational environment. The atmospheric correction of ASTER data has two distinct methods, one for the TIR and the

other for the solar reflective. The TIR approach is based on the radiative transfer code MODTRAN and relies on atmospheric temperature and humidity profiles derived from MODIS data or global assimilation models. The solar reflective approach is an LUT method based on results from a Gauss–Seidel iteration radiative transfer code.

The solar-reflective approach is also being developed to include adjacency effects. This algorithm is simulated by a checkerboard type surface, whose pixels may be composed of either land or water and considers effects within an area of 20×20 km. Numerical simulations of this algorithm reveal that the adjacency effect depends upon the vertical profile of the atmospheric constituents, is larger in clear conditions than in hazy conditions, is larger with higher land reflectance, and is small over land in coastal zones. The radiance over a lake inside the continent can be derived to simulate the surface of which pixels are either lake or land. It is not essential for it to be either a Lambertian or Cox–Munk model water surface.

Sensitivity analyses of the results of the atmospheric correction indicate that the solar reflective correction will be limited by the accuracy of the input parameters and should be no better than results obtained from using ground-based atmospheric data. The expected uncertainty of the solar reflective should be 0.02 in reflectance at reflectances less than 0.1. This uncertainty in reflectance rises to 0.04 at a reflectance of 0.5. It is difficult at this time to assess numerical values to the uncertainty of the TIR correction. One general conclusion is that obtaining surface radiance uncertainty below the 1-K accuracy of the ASTER instrument itself will be difficult for warm, humid atmospheres.

REFERENCES

[1] H. Fujisada and A. Ono, "Overview of ASTER design concept," in *Proc. SPIE,* 1990, vol. 1490, pp. 244–268.
[2] H. Fujisada, "Overview of ASTER instrument on EOS AM-1 platform," in *Proc. SPIE,* 1994, vol. 2268, pp. 14–36.
[3] ——, "ASTER sensor system," *Jpn. J. Remote Sensing,* vol. 15, pp. 1–15, 1995.
[4] A. Ono, F. Sakuma, K. Arai, Y. Yamaguchi, H. Fujisada, P. Slater, K. Thome, F. Palluconi, and H. Kieffer, "Preflight and in-flight calibration plan for ASTER," *J. Atmos. Ocean. Technol.,* vol. 13, pp. 322–335, 1996.
[5] Y. Yamaguchi, A. B. Kahle, H. Tsu, T. Kawakami, and M. Pniel, "Overview of Advanced Spaceborne Thermal Emission and Reflection Radiometer (ASTER)," this issue, pp. 1062–1071.
[6] A. B. Kahle, F. Palluconi, S. Hook, V. J. Realmuto, and G. Bothwell, "Advanced Spaceborne Thermal Emission and Reflection Radiometer (ASTER)," *Int. J. Imaging Syst. Technol.,* vol. 3, pp. 144–151, 1991.
[7] Y. Yamaguchi, H. Tsu, and H. Fujisada, "A scientific basis of ASTER instrument design," in *Proc. SPIE,* 1993, vol. 1939, pp. 150–160.
[8] P. M. Teillet, "An algorithm for the radiometric and atmospheric correction of AVHRR data in the solar reflective," *Remote Sens. Environ.,* vol. 41, pp. 185–195, 1992.
[9] R. S. Fraser, O. P. Bahethi, and A. H. Al-Abbas, "The effect of the atmosphere on the classification of satellite observations to identify surface features," *Remote Sens. Environ.,* vol. 6, pp. 229–249, 1977.
[10] Y. J. Kaufman, "The atmospheric effect on the separability of field classes measured from satellites," *Remote Sens. Environ.,* vol. 18, pp. 21–34, 1985.
[11] D. S. Kimes and P. J. Sellers, "Inferring hemispherical reflectance of the earth's surface for global energy budgets from remotely sensed nadir or directional radiance values," *Rem. Sens. Environ.,* vol. 18, pp. 205–223, 1985.
[12] M. S. Moran, R. D. Jackson, G. F. Hart, P. Slater, R. J. Bartell, S. F. Biggar, D. I. Gellman, and R. P. Santer, "Obtaining surface reflectance factors from atmospheric and view angle corrected SPOT-1 HRV data," *Remote Sens. Environ.,* vol. 32, pp. 203–214, 1990.
[13] H. R. Gordon, D. K. Clark, J. L. Mueller, and W. A. Hovis, "Phytoplankton pigments derived from the Nimbus-7 CZCS: Initial comparisons with surface measurements," *Science,* vol. 210, pp. 63–66, 1980.
[14] H. R. Gordon, "Atmospheric correction of ocean color imagery in the Earth observing system era," *J. Geophys. Res.,* vol. 102, pp. 17 081–17 106, 1997.
[15] *J. Geophys. Res.,* vol. 102, pp. 16 815–17 217, 1997.
[16] J. E. Hilland *et al.,* "Production of global sea surface temperature fields for the Jet Propulsion Laboratory workshop comparisons," *J. Geophys. Res.,* vol. 90, pp. 11 642–11 650, 1985.
[17] C. Prabhakara *et al.,* "Estimation of sea surface temperature from remote sensing in the 11 and 13 μm window region," *J. Geophys. Res.,* vol. 79, pp. 5039–5044, 1975.
[18] L. M. McMillin, "Estimation of sea surface temperature from two infrared window measurements with different absorption," *J. Geophys. Res.,* vol. 90, pp. 11 587–11 600, 1975.
[19] P. Deschamps and T. Phulpin. "Atmospheric correction of infrared measurements of sea surface temperature using channels at 3.7, 11, and 12 μm," *Boundary Layer Meteorol.,* vol. 18, pp. 131–143, 1980.
[20] J. C. Price, "Land surface temperature measurements from the split window channels of the NOAA 7 Advanced Very High Resolution Radiometer," *J. Geophys. Res.,* vol. 89, pp. 7231–7237, 1984.
[21] E. Kalnay *et al.,* "Global numerical weather prediction at NMC," *Bull. Amer. Meteorol. Soc.,* vol. 70, pp. 1410–1428, 1990.
[22] S. D. Schubert *et al.,* "An assimilated dataset for earth science applications," *Bull. Amer. Meteorol. Soc.,* vol. 74, pp. 2331–2342, 1993.
[23] D. B. Gesch, "Topographic data requirements for EOS global change research," U.S. Geological Survey, Washington, DC, 1994, p. 60.
[24] R. G. Holm, R. D. Jackson, B. Yuan, M. S. Moran, P. Slater, and S. F. Biggar, "Surface reflectance factor retrieval from thematic mapper data," *Remote Sens. Environ.,* vol. 27, pp. 47–57, 1989.
[25] P. Slater and R. D. Jackson, "Atmospheric effects on radiation reflected from soil and vegetation as measured by orbital sensors using various scanning directions," *Appl. Opt.,* vol. 21, pp. 3923–3931, 1982.
[26] M. S. Moran, R. D. Jackson, P. Slater, and P. M. Teillet, "Evaluation of simplified procedures for retrieval of land surface reflectance factors from satellite sensor output," *Remote Sens. Environ.,* vol. 41, pp. 169–184, 1992.
[27] R. S. Fraser, S. Mattoo, E.-N. Yeh, and C. R. McClain, "Algorithm for atmospheric and glint corrections of satellite measurements of ocean pigment," *J. Geophys. Res.,* vol. 102, pp. 17 107–17 118, 1997.
[28] L. L. Stowe, A. M. Ignatov, and R. R. Singh, "Development, validation, and potential enhancements to the second-generation operational aerosol product at the National Environmental Satellite, Data, and Information Service of the National Oceanic and Atmospheric Administration," *J. Geophys. Res.,* vol. 102, pp. 16 923–16 934.
[29] R. S. Fraser, R. A. Ferrare, Y. J. Kaufman, B. L. Markham, and S. Mattoo, "Algorithm for atmospheric correction of aircraft and satellite imagery," *Int. J. Remote Sensing,* vol. 13, pp. 541–557, 1992.
[30] B. M. Herman and S. R. Browning, "A numerical solution to the equation of radiative transfer," *J. Atmos. Sci.,* vol. 22, pp. 559–566, 1965.
[31] A. Murray, B. Eng, and K. Thome, "Implementation of a very large atmospheric correction lookup table for ASTER using a relational database management system," in *Proc. SPIE,* 1996, vol. 2820, pp. 245–258.
[32] J. Lenoble, *Radiative Transfer in Scattering and Absorbing Atmospheres: Standard Computational Procedures.* Hampton, VA: Deepak, 1985, p. 300.
[33] Y. Mekler and Y. J. Kaufman, "The effect of earth's atmosphere on contrast reduction for a nonuniform surface albedo and 'two-halves' field," *J. Geophys. Res.,* vol. 85, pp. 4067–4083, 1980.
[34] ——, "Contrast reduction by the atmosphere and retrieval of nonuniform surface reflectance," *Appl. Opt.,* vol. 21, pp. 310–316, 1982.

[35] D. J. Diner and J. V. Martonchik, "Atmospheric transfer of radiation above an inhomogeneous non-Lambertian reflective ground-2 computational considerations and results," *J. Quant. Spectrosc. Radiat. Transf.,* vol. 32, pp. 279–304, 1984.

[36] D. Tanré, M. Herman, and P. Y. Deschamps, "Influence of the background contribution upon space measurements of ground reflectance," *Appl. Opt.,* vol. 20, pp. 3676–3684, 1981.

[37] T. Takashima and K. Masuda, "Operational procedure of atmospheric correction on satellite visible data allowing for the adjacency effect," in *Proc. SPIE,* 1996, vol. 2817, pp. 70–81.

[38] ——, "Simulation of atmospheric effects on the emergent radiation over a checkerboard type of terrain," *Astrophys. Space Sci.,* vol. 198, pp. 253–263, 1992.

[39] ——, "A new approach to evaluation of the effect of the two half-Lambert surfaces composed of different albedos on the emergent radiation at the top of the atmosphere," *Astrophys. Space Sci.,* vol. 196, pp. 45–55, 1992.

[40] F. X. Kneizys, E. P. Shettle, L. W. Abreu, J. H. Chetwynd, G. P. Anderson, W. O. Gallery, J. E. A. Selby, and S. A. Clough, *User Guide to LOWTRAN 7,* Air Force Geophys. Lab., Hanscom AFB, MA, AFGL-TR-88-0177, 1988, p. 146.

[41] IAMAP, "A preliminary cloudless standard atmosphere for radiation computation," Boulder, CO, 1982, sec. 2, pp. 78–107,.

[42] J. E. A. Selby and R. M. McClatchey, "Atmospheric transmittance from 0.25–28.5 μm: Computer code LOWTRAN2," Air Force Cambridge Res. Lab., Cambridge, MA, AFCRL-72-0745, 1972.

[43] Y. J. Kaufman, D. Tanré, L. A. Remer, E. Vermote, A. Chu, and B. N. Holben, "Operational remote sensing of tropospheric aerosol over land from EOS Moderate Resolution Imaging Spectroradiometer," *J. Geophys. Res.,* vol. 102, pp. 17 051–17 068, 1997.

[44] Y. J. Kaufman and C. Sendra, "Algorithm for automatic atmospheric corrections to visible and near-IR satellite imagery," *Int. J. Remote Sensing,* vol. 8, pp. 1357–1381.

[45] F. Becker, "The impact of spectral emissivity on the measurement of land surface temperature from a satellite," *Int. J. Remote Sensing,* vol. 8, pp. 1509–1522, 1987.

[46] Z. Wan and J. Dozier, "Effects of temperature-dependent molecular absorption coefficients on the thermal infrared remote sensing of the earth surface," in *Proc. IGARSS,* 1992, pp. 1242–1244.

[47] L. W. Abreu, "MODTRAN," in *Proc. 1991 Battlefield Atmos. Conf.,* 1991.

[48] G. P. Anderson, "MODTRAN2: Suitability for remote sensing," in *Proc. Workshop Atmos. Correction Landsat Imagery,* 1993.

[49] L. S. Rothman *et al.,* "The HITRAN molecular database: Editions of 1991 and 1992," *J. Quant. Spectrosc. Radiat. Transfer,* vol. 48, p. 469, 1992.

[50] S. A. Clough *et al.,* "FASCOD3: Spectral simulation," in *Proc. Int. Radiat. Symp.* Hampton, VA: Deepak, 1988.

K. Thome, photograph and biography not available at the time of publication.

F. Palluconi, photograph and biography not available at the time of publication.

T. Takashima, photograph and biography not available at the time of publication.

K. Masuda, photograph and biography not available at the time of publication.